LAWRENCE
LIVERMORE
NATIONAL
LABORATORY

LLNL-TR-661699

Modeling the mechanical and aging properties of silicone rubber and foam - stockpile-historical & additively manufactured materials

A. Maiti, T. H. Weisgraber, R. H. Gee

September 30, 2014

Disclaimer

This work performed under the auspices of the U.S. Department of Energy by Lawrence Livermore National Laboratory under Contract DE-AC52-07NA27344.

WBS 5.1.4
Modeling the mechanical and aging properties of silicone rubber and foam – stockpile-historical & additively manufactured materials

Amitesh Maiti, Todd Weisgraber, Richard H. Gee

WBS Deliverable

1.1 Introduction

Within the scope of ESC-NNM the major task has been to understand how the mechanical properties (modulus, permanent set, load retention) change over long periods of time (often decades) under stockpile conditions. In previous years the focus has been on historical (legacy) materials that are already in deployment. Beginning last year, our efforts have extended to cover both legacy as well as new materials that are being synthesized by additive manufacturing techniques. We follow a two-prong approach to modeling foams: a constitutive approach in which the foam material is considered as a compressible continuum, and a finite-element modeling (FEM) of the foam microstructure using an incompressible constitutive model for the constituent rubber. The microstructure information is precisely known for the additively manufactured material, while for the legacy system it is obtained from X-ray CT images. Our efforts in FY13-14 can be broken down into several different projects:

(1) Modeling the radiation-induced aging of Dow Corning rubber SE 1700 under tensile strain;

(2) Aging models for legacy foams M97* and M9763 from elevated temperature data under various compression levels;

(3) Finite element analysis of M9763 aged in a desiccating environment.

1.2 Radiation-aging model for Dow Corning elastomer SE 1700 under tensile strain

1.2.1 Background

Dow Corning SE 1700 is a silicone elastomer that is being used to fabricate patterned functional structures by direct ink writing, an additive 3D printing technique in which the uncured material is deposited through a nozzle in a layer-by-layer fashion, followed ultimately by a curing step after all layers are deposited. Permanent set, tensile strength, elongation at break, and Young's modulus were measured as a function of radiation dose under a tensile "aging" strain. From the measurements, a complete phenomenological model of the stress response as a function of radiation dose and aging strain was developed. The basis for constructing the model is likely applicable to other reinforced silicones. This work will allow changes in the mechanical properties caused by irradiation under strain to be taken into account during the initial stages of component design for a given application.

1.2.2 Measurements

Experimental details are laid out in ref. [1]. Here we report on the main results.

Permanent set for the aged SE 1700 increased with radiation dose and aging strain (Fig. 1). This effect has been reported previously for other commercial filled silicone elastomers [2-4].

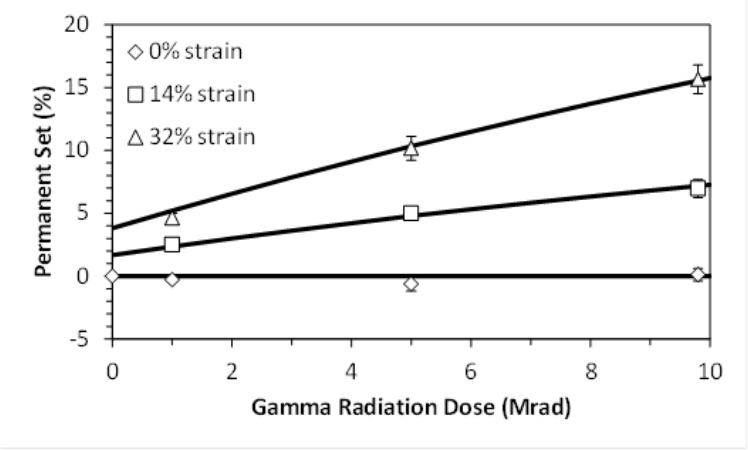

Fig. 1. Average permanent tensile set (measured using bench marks) of accelerated aged SE 1700 for various radiation doses and aging strains. The solid lines were generated using the model given by Eqs. (1.2.6) and (1.2.7). See text.

Dividing the permanent set by the aging strain yields the "relative permanent set," which essentially removes the dependence on aging strain (Fig. 2). The radiation dose dependence of SE 1700 is similar to that of other previously tested commercial filled silicone elastomers, Dow Corning TR-55 and Dow Corning DC-745U (Fig. 2). However, the SE 1700 curves in Figs. 1 and 2 appear to be shifted vertically such that they do not intercept the origin. This is, at least in part, likely an artifact stemming from the relatively

short time (30 min) between removal of the aging strain and measurement of the permanent set compared to that used in the previous tests (24 h). Though most of the recovery occurred nearly instantaneously after removal of the aging strain, recovery may continue very slowly over several days at room temperature [5, 6].

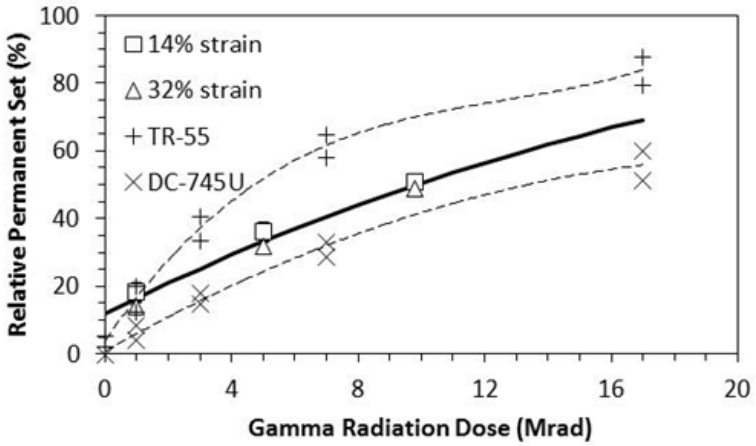

Fig. 2. Relative permanent set (normalized by aging strain) of SE 1700 compared to other commercial filled silicone elastomers, TR-55 (data from Ref. [3]) and DC-745U (data from Ref. [4]). The TR-55 was subjected to aging strains of 20-47% and the DC-745U was subjected to aging strains of 20-40%. Error bars represent standard deviation (n = 4). The solid line was generated using the model given by Eqs. (1.2.6) and (1.2.7). The dashed lines illustrate trends in the TR-55 and DC-745U data.

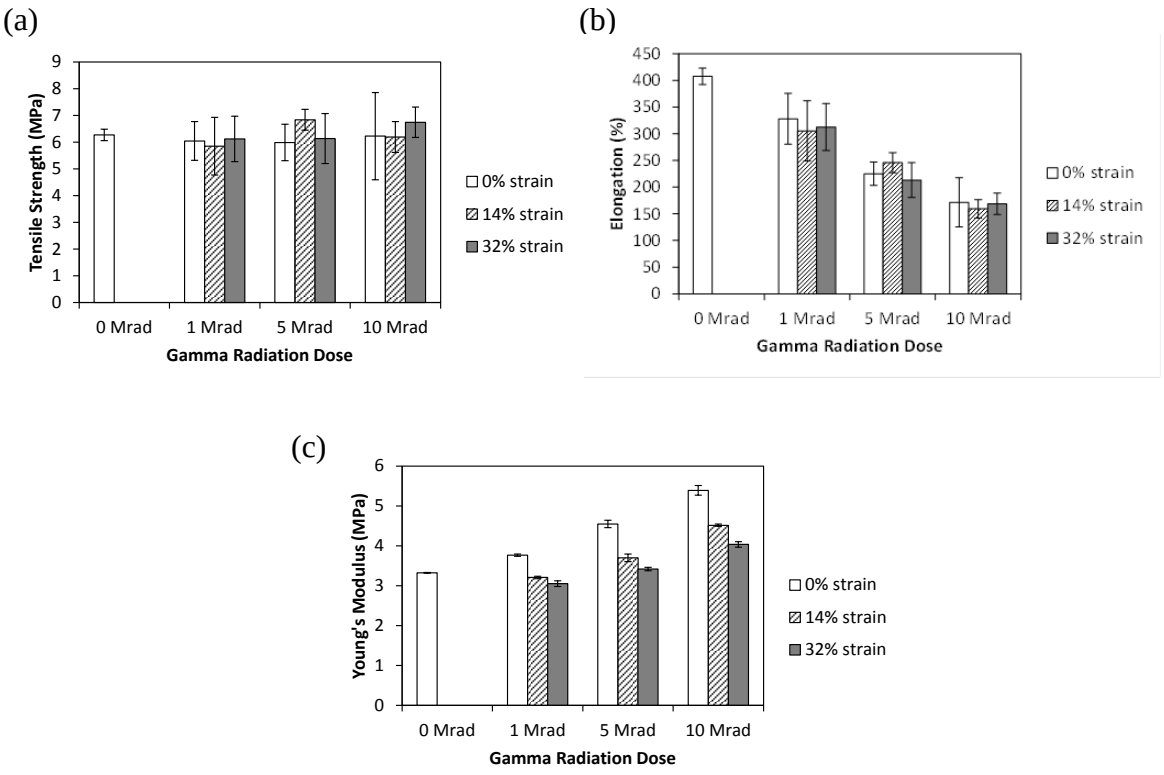

Fig. 3. Average (a) tensile strength at break, (b) elongation at break, and (c) Young's modulus of accelerated aged SE 1700 for various radiation doses and aging strains. Error bars represent standard deviation (# samples = 4).

Average strength (engineering stress at break), elongation at break, and Young's modulus of aged SE 1700 are given in Fig. 3. The specimens did not yield before breaking. The strength (~6 MPa) was essentially independent of radiation dose and aging strain. However, elongation decreased and Young's modulus increased with radiation dose, indicating radiation-induced hardening of the material. Radiation hardening due to crosslink formation has been reported previously for other commercial filled silicone elastomers [2-4, 7]. Aging strain had the opposite effect, causing softening of the material (Mullins effect [8]). The interplay of opposing effects of radiation and aging strain has been investigated previously [2, 4]. The stress vs. strain curves in Fig. 4 further illustrate the opposing effects of radiation and aging strain.

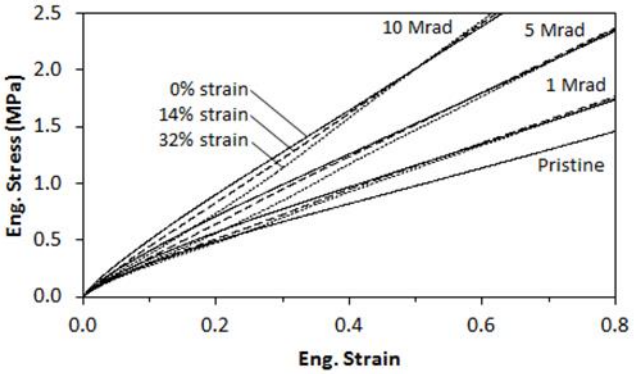

Fig. 4. Stress vs. strain of accelerated aged SE 1700 for various radiation doses and aging strains. Solid line: 0% strain; large dashes: 14% strain; small dashes: 32% strain.

1.2.3 Modeling

For an incompressible material under not-too-large uniaxial deformation, a commonly employed model of stress response is the neo-Hookean model given by:

$$\sigma = \frac{E}{3}\left(\lambda^2 - \frac{1}{\lambda}\right) \tag{1.2.1}$$

where σ is the true stress, E is the Young's modulus, and λ is the uniaxial stretch ratio (stretched specimen length divided by original length). The Neo-Hookean model fits to the experimental stress-strain data (up to 50% strain) for pristine and irradiated specimens at 0% aging strain.

Extending the work of Maiti *et al.* [2, 3] for a polymer irradiated under strain, the aged polymer can be described by two independent networks in accordance with Tobolsky *et al.* [9, 10]. Part of the original network (network #1) is modified by radiation-induced crosslinking, which leads to the formation of a new network (network #2) that is at equilibrium in the stretched condition. The resulting (true) stress response of these two networks is given by

$$\sigma = \frac{E_0}{3}\frac{(1+C_0D)}{1+f_{\text{eff}}}\frac{1}{f_M}\left[\left(\lambda'^2 - \frac{1}{\lambda'}\right) + f_{\text{eff}}\left(\lambda''^2 - \frac{1}{\lambda''}\right)\right] \tag{1.2.2}$$

where E_0 is the Young's modulus of the pristine material, D is the radiation dose, C_0 is a constant (fit parameter) describing the dependence of the Young's modulus on the radiation dose, f_{eff} is a function accounting for the effect of the radiation-induced crosslinking (f_{eff}=0 for D=0), λ' and λ'' are the uniaxial stretch ratios in the original and newly formed networks, respectively, and f_M is an additional function to account for softening due to the Mullins effect. The uniaxial stretch ratios in Eq. (1.2.2) are given by

$$\lambda' = \frac{\lambda}{1 + C_1(\lambda_1 - 1)} \tag{1.2.3}$$

and

$$\lambda'' = \frac{\lambda'}{\lambda_1} \tag{1.2.4}$$

where the denominators represent the equilibrium stretch ratios of the networks and C_1 is a constant (fit parameter) describing the dependence of the equilibrium length of the original network on the aging strain. Following recent work [11], the Mullins softening function, f_M, is proposed to decrease linearly (for simplicity) with aging strain:

$$f_M = 1 + C_2(\lambda_1 - 1) \tag{1.2.5}$$

where C_2 is a constant. Note, however, that this model is valid only for strain levels up to the previously attained maximum strain (*i.e.*, λ_1). Once this strain is exceeded, the material response follows the first loading curve, where Mullins softening is not present. Also, for high strain levels one needs to take into account complexities due to non-Gaussian effects, such as local strain amplification, as discussed by Maiti, *et al.* [11]. For λ_1=1 (no aging strain), Eq. (1.2.2) reverts back to Eq. (1.2.1) with $E=E_0(1+C_0D)$. Fitting this expression to the measured Young's modulus at 0% aging strain vs. radiation dose data yields C_0=0.101 Mrad^{-1}.

In the previous work by Maiti *et al.* [2, 3] for a different material (Dow Corning TR-55), the denominator in Eq. (1.2.3) (*i.e.*, the equilibrium length of the original network) was taken to be 1. The TR-55 material showed no permanent deformation after aging under strain (before radiation exposure), which is given by the case C_1=0. This was not the case for SE 1700, as suggested by the permanent set data in Fig 1. Hence, the equilibrium length of the original network was permitted to increase with aging strain; a linear function was chosen for simplicity.

At zero stress after aging (*i.e.*, full relaxation), the stress response given by the two-stage independent network model in Eqs. (1.2.2)-(1.2.5) predicts a recovered stretch ratio

$$\lambda_s = \left[1 + C_1(\lambda_1 - 1)\right]\left(\frac{1 + f_{\text{eff}}\lambda_1}{1 + f_{\text{eff}}/\lambda_1^2}\right)^{1/3} \tag{1.2.6}$$

The function f_{eff}, which is an increasing function of the radiation dose, D [2, 3], was proposed to have the form

$$f_{\text{eff}} = \exp(C_3 D) - 1 \tag{1.2.7}$$

where C_3 is a constant. After putting it in terms of the relative permanent set (*i.e.*, normalizing by the aging strain), Eq. (1.2.6) was fit to the experimental relative permanent set vs. radiation dose data in Fig. 2 to yield C_1=0.119 and C_3=0.055 Mrad^{-1}. Equation (1.2.6) can be rearranged to solve for f_{eff} for the experimental values of λ_1 and λ_s in Fig. 1. These values of f_{eff} are plotted vs. radiation dose in Fig. 5 along with the curve generated by Eq. (1.2.7). As previously observed for Dow Corning TR-55 [2, 3], f_{eff} is largely independent of λ_1 and is an increasing function of D only.

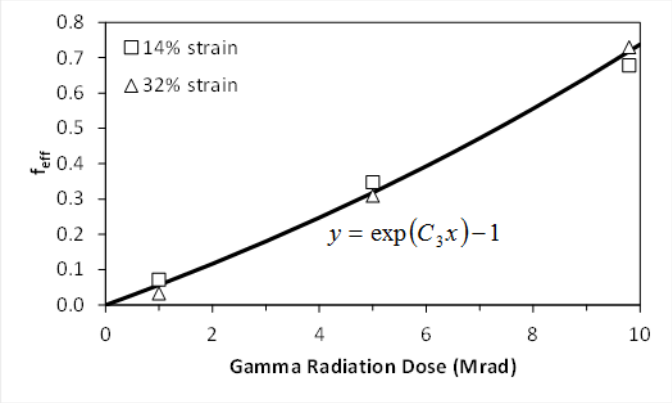

Fig. 5. Values of the function f_{eff} vs. gamma radiation dose data for $\lambda_1 > 1$. The function is independent of aging strain. The curve generated by Eq. (1.2.7) is given by the solid line (C_3=0.055 Mrad^{-1}).

1.2.4 Discussion

Mechanical property changes occurred in SE 1700 silicone elastomer irradiated under tensile strain. Permanent set increased with radiation dose and aging strain. The tensile strength at break (~ 6 MPa) was essentially independent of the radiation dose and aging strain. However, elongation at break decreased and Young's modulus increased with radiation dose, indicating radiation-induced hardening (crosslinking) of the material. Aging strain had the opposite effect, causing softening of the material (Mullins effect). These changes in mechanical properties could affect the functionality of solid SE 1700 components, as well as 3D structures fabricated from SE 1700 by direct ink writing. The results of this study provide insight into component performance over time, and may guide component/system design to potentially mitigate the effects of irradiation and aging strain. The 3D printing technique provides the unique opportunity to engineer the mechanical response by controlling the design of the structure (e.g., strand diameter, spacing, orientation, etc.), potentially providing an additional means of compensating for permanent set and changes in the stress response as the material ages.

To provide a predictive capability regarding the impact of aging on the mechanical properties of SE 1700, a phenomenological model of the stress response as a function of radiation dose and aging strain was developed. A two-stage independent network model was modified to include radiation dose-dependent factors accounting for radiation-induced hardening and permanent set based on experimental measurements. In addition, a strain-dependent Mullins softening factor was included to obtain good agreement with

the experiment. This model can likely be extended to other reinforced silicone elastomers.

1.3 Thermal-aging models for legacy foams M9763 and M97* from elevated temperature data at various compression levels

1.3.1 Background

M97* and M9763 belong to the M97xx series of cellular silicone materials that have been deployed as stress cushions in some of the LLNL systems. Their purpose of these support foams is to distribute the stress between adjacent components, maintain relative positioning of various components, and mitigate the effects of component size variation due to manufacturing and temperature changes. In service these materials are subjected to a continuous compressive strain over long periods of time. In order to ensure their effectiveness, it is important to understand how their mechanical properties change over time. The properties we are primarily concerned about are: compression set, load retention, and stress-strain response (modulus).

1.3.2 Experiment

With the aim of predicting the changes in the above properties under long-term deployment (decades), a 24-month-long accelerated aging study has been conducted on both these foams. Some of the details of these experiments include: (1) cylindrical sample disks of diameter 29 mm and thickness of 3 mm); (2) four different temperatures (room temperature, 35 ºC, 50 ºC, 70 ºC); (3) multiple compressive strains for M97* (15, 30, and 55%) and a single compressive strain for M9763 (25%); (4) a dry nitrogen atmosphere, in order to prevent oxidation reactions at elevated temperatures; (5) monthly unload/load cycles for mechanical measurements in ambient air, followed by returning the sample to dry nitrogen atmosphere for continued aging. Fig. 6 displays a schematic diagram that explains how compression set and load retention were defined in our measurements.

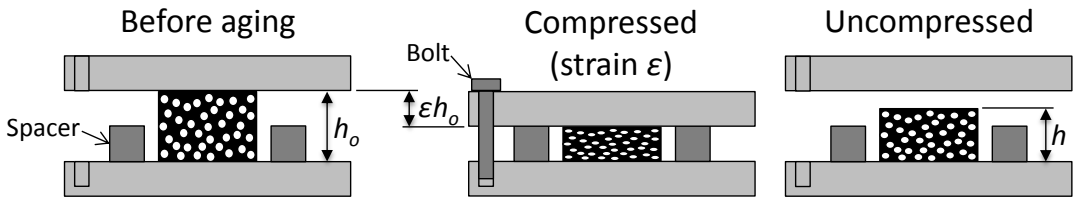

Fig. 6. Schematic diagram of our measurements: compression set is defined as: $C_S = (h - h_0)/(\varepsilon h_0)$, while load retention is defined as: $L_R = F(t)/F(0)$, where $F(t)$ is the force at time t necessary to compress the pad to an engineering strain of ε.

1.3.3 Results and aging model

Fig. 7 and 8 display the compression set results for M9763 and M97* respectively.

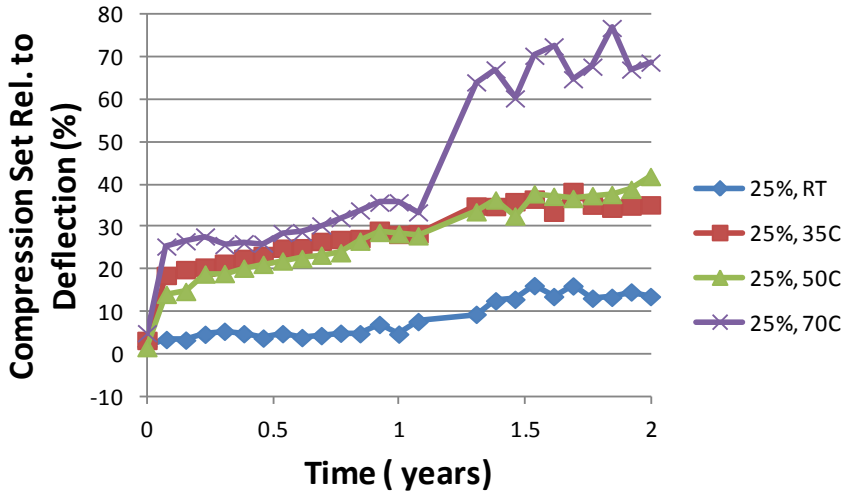

Fig. 7. Compression set results for foam M9763 performed at an engineering compressive strain of $\varepsilon = 25\%$.

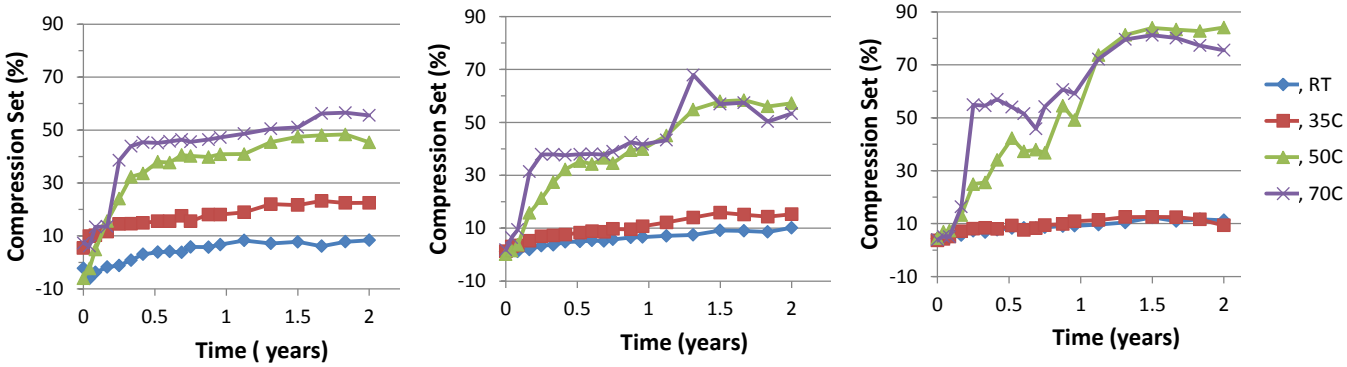

Fig. 8. Compression set results for foam M97* performed at engineering compressive strains of $\varepsilon = 25\%$ (left), 30% (middle), and 55% (right).

From the data we immediately see that there are discrepancies both as a function of time and as a function of temperature. Possible reasons could include operator errors involving, e.g., maintaining the required temperature, or perhaps different aging mechanisms, e.g., moisture outgassing effects at elevated temperatures, etc. In spite of the discrepancies, we also see significant differences between the aging behaviors of M97* and M9763.

Two of the common methods for long-term aging estimates include: (1) time-temperature superposition (TTS), in which the experimental curves at various temperatures are shifted along the logarithmic time-axis in order to generate a single master curve [12]; and (2) a kinetic model in which the rate constant is assumed to follow the Arrhenius behavior [13]. While TTS results are being reported separately by Ward Small, we report here results using kinetic models.

Previously, similar data on S5370 foam at $\varepsilon = 50\%$ was modeled using a first order kinetic model [13] defined by the following equations:

$$C_S(t) = 1 - e^{-kt}\,, \qquad (1.3.1)$$

where k is a kinetic rate constant, which is assumed to follow the Arrhenius behavior:

$$k = Ae^{-\Delta E/k_B T}\,, \qquad (1.3.2)$$

A being a pre-factor, ΔE an activation energy, k_B the Boltzmann constant, and T the absolute temperature. However, we found that the compression set data of M97* and M9763 as well their load retention data (discussed below) are not described well by the first order model. Thus, we considered two different modifications of eq. (1.3.1). The first model, called the modified exponential model below, is defined by the formula:

$$C_S(t) = 1 - e^{-kt^n}\,, \qquad (1.3.3)$$

where n is a positive real number that can be greater or less than 1. The second model on the other hand, called the O(n) model below, is defined by the formula:

$$C_S(t) = 1 - \{1 + (n-1)kt\}^{-1/(n-1)}\,, \qquad (1.3.4)$$

where n, the order of the reaction, is a positive real number (> or < 1, but $\neq 1$).

M9763 (compression set)

Fig. 9 displays the results for fitting the compression set data of M9763 with the modified exponential and O(n) models. The T = 35 °C data was inconsistent with the rest of the data, and was therefore removed from the anaysis.

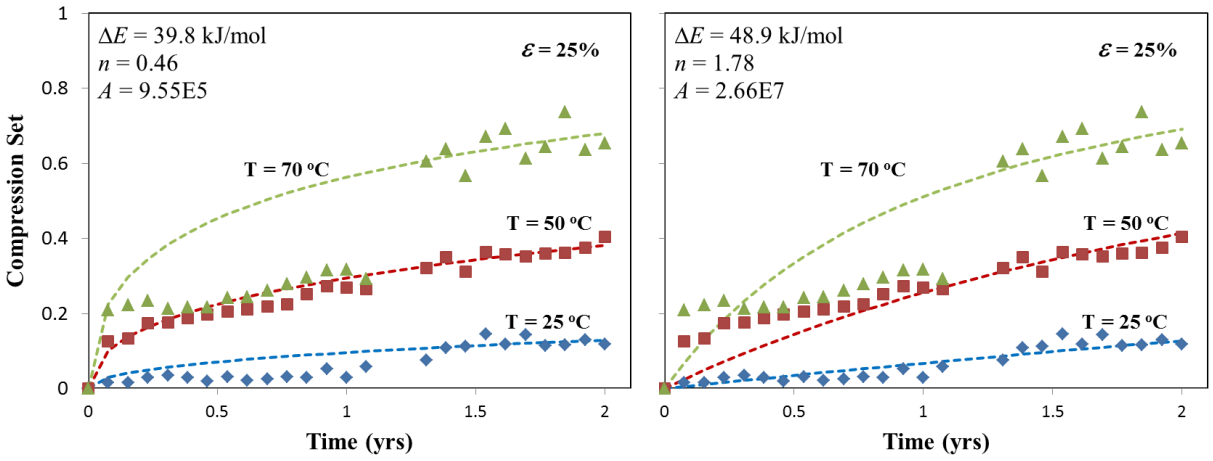

Fig. 9. M9763: Best fits to the compression set data using: (left) the modified exponential model; and (right) the O(n) model.

Given the different slopes of the fits from the two aging models, it is not surprising that they yield different long-term aging predictions under ambient conditions (25 °C). See Fig. 10 below.

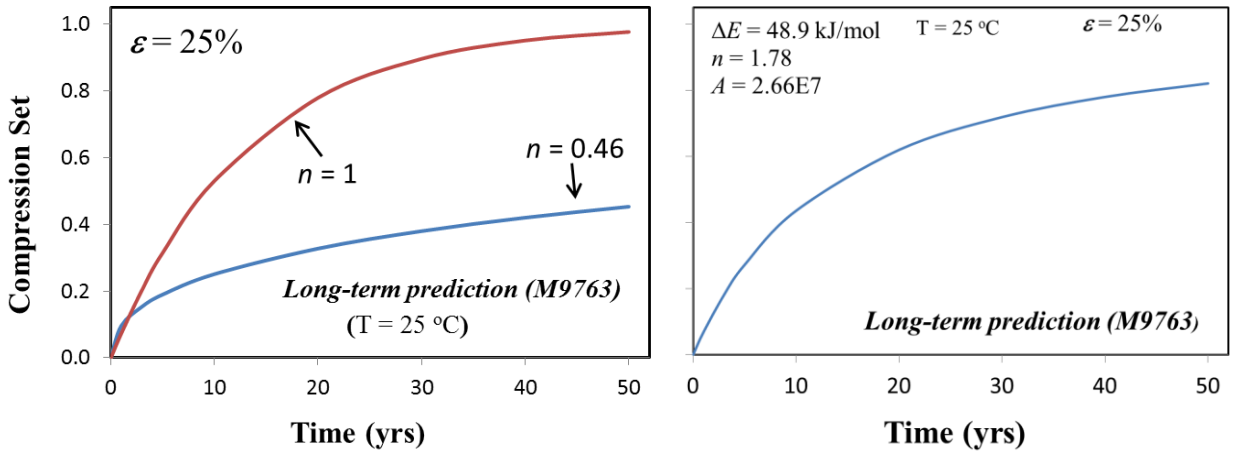

Fig. 10. M9763: Long-term predictions for compression set using: (left) the modified exponential model; and (right) the O(*n*) model.

M97* (compression set)

The best fits to the compression set results for M97* are displayed in Fig. 11. The T = 70 °C data was inconsistent with the rest, and was thus removed from analysis.

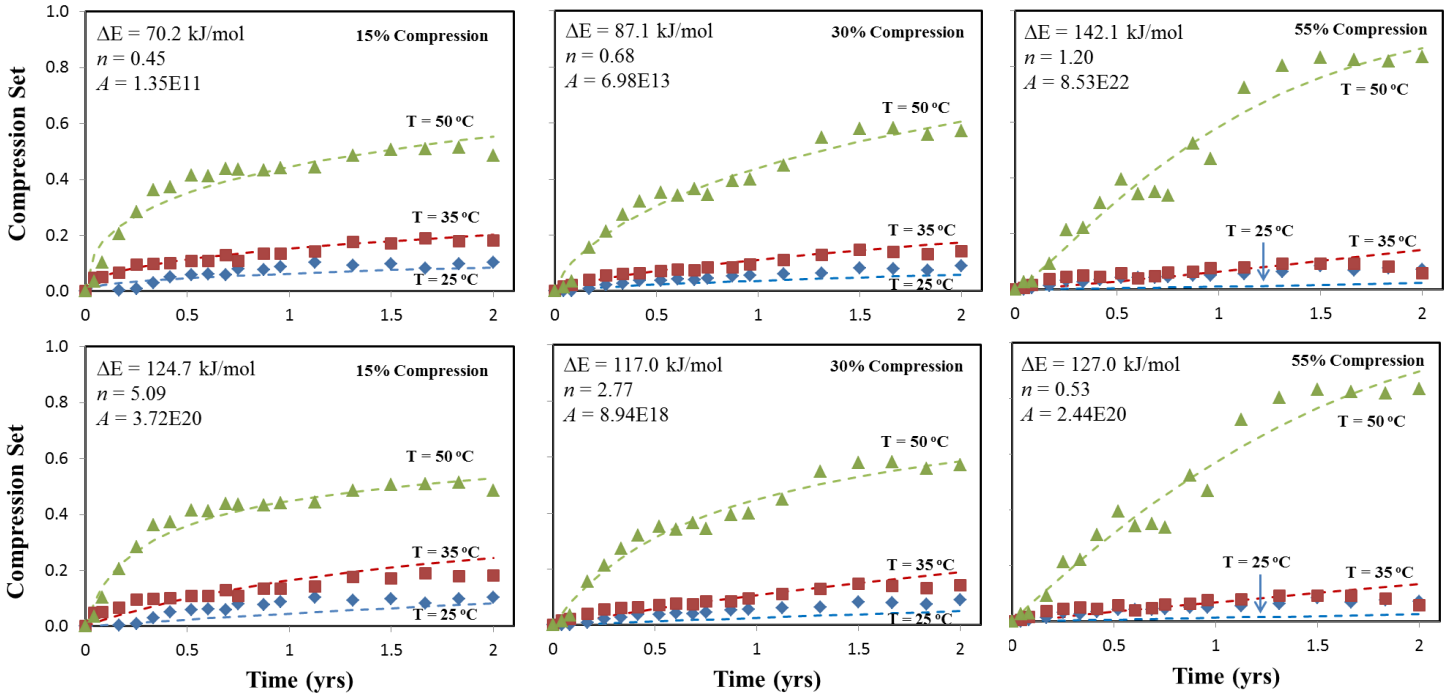

Fig. 11. M97*: Best fits to the compression set data using: (top) the modified exponential model; and (bottom) the O(*n*) model.

Fig. 12 displays the long-term aging predictions under ambient conditions (25 °C) for M97*. Interestingly, the O(*n*) model predicts compression set that is largely insensitive to the aging compression level (ε) over a period of 50 years.

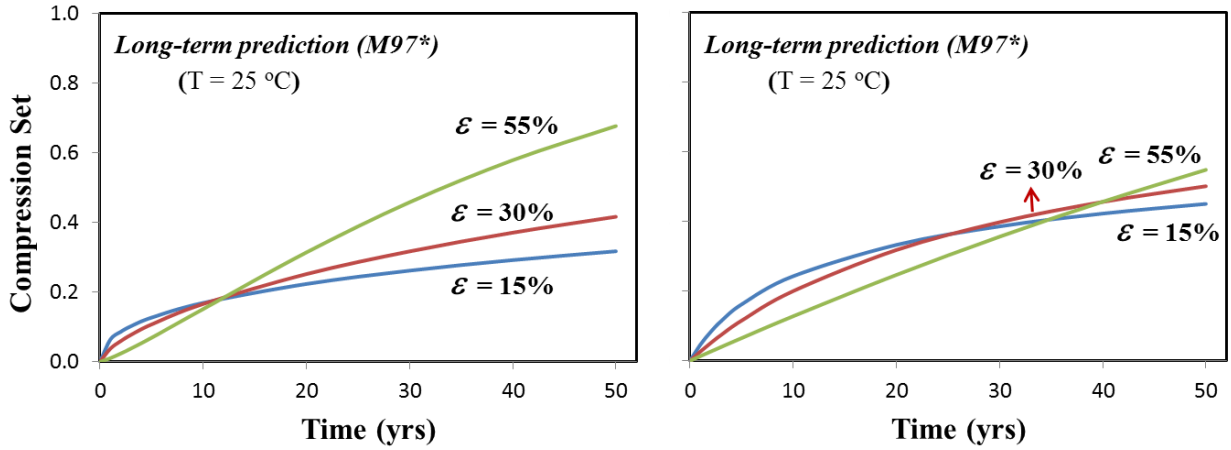

Fig.12. M97*: Long-term predictions for compression set using: (left) the modified exponential model; and (right) the O(*n*) model.

Load Retention:

Similar to permanent set, the evolution of load retention was also modeled using the modified exponential and O(*n*) functions, as described below:

$$L_R(t) = e^{-kt^n}\,, \qquad (1.3.5)$$

$$L_R(t) = \{1 + (n-1)kt\}^{-1/(n-1)}\,, \qquad (1.3.6)$$

where k follows the Arrhenius behavior given by eqn. (1.3.2) with different A and ΔE parameters as compared to those for compression set.

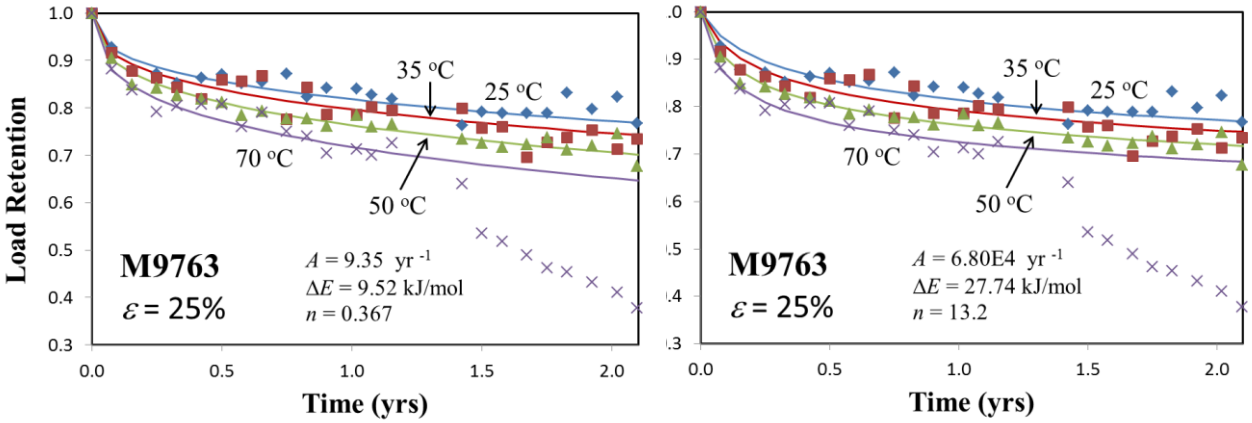

Fig. 13. M9763: Best fits to the load retention data using: (left) the modified exponential model; and (right) the O(*n*) model. The second year data at T = 70 °C was removed from the analysis.

Fig. 13 displays the best fits to the load retention data of M9763 using the two aging models, while Fig. 14 shows the long-term predictions.

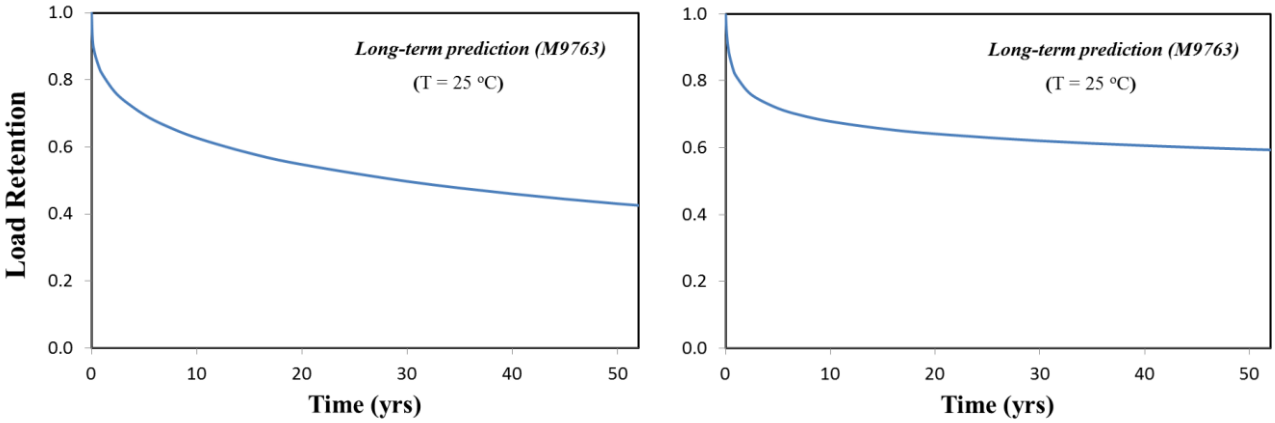

Fig. 14. M9763: Long-term predictions for load retention using: (left) the modified exponential model; and (right) the O(*n*) model.

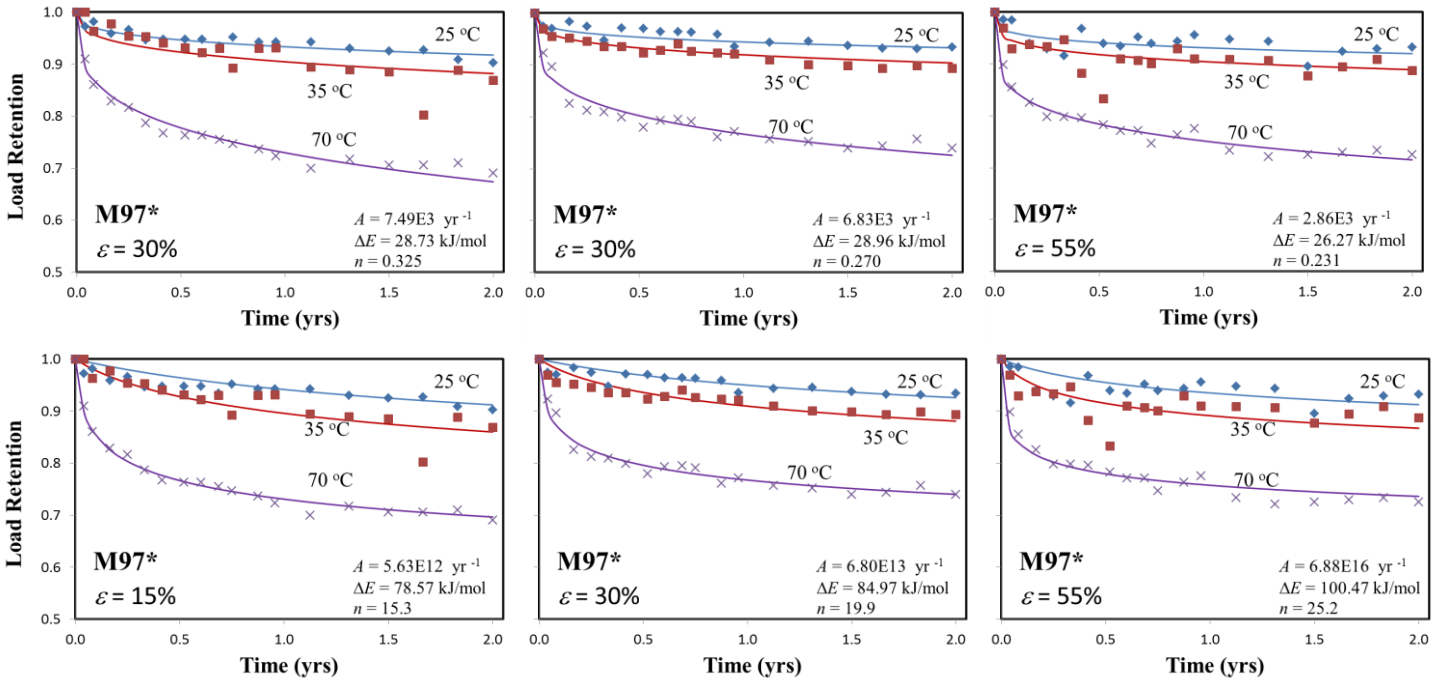

Fig. 15. M97*: Best fits to the load retention data using: (top) the modified exponential model; and (bottom) the O(*n*) model. Due to inconsistencies, the T = 50 °C data was removed from analysis.

Fig. 15 displays the best fit to the load retention data for M97* and Fig. 16 displays the long-term predictions at T = 25 °C. Interestingly, both models yield almost identical results and indicate that L_R is fairly insensitive to the aging strain.

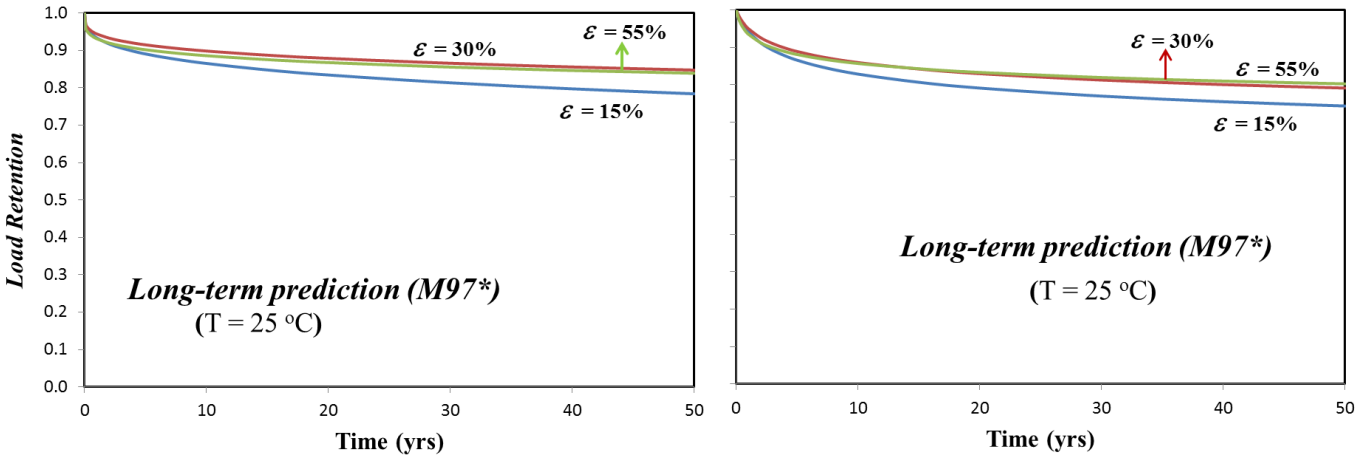

Fig. 16. M97*: Long-term predictions for load retention using: (left) the modified exponential model; and (right) the O(n) model.

1.3.4 Discussion

In this section we analyzed 2-year-long aging data on legacy foams M9763 and M97*. The focus was on compression set (C_S) and load retention (L_R) and how they evolve as a function of time at four different temperatures: 25, 35, 50, and 70 °C. Given that there are large uncertainties in the application of the time-temperature superposition (TTS) of the data, we attempted two different kinetic models for aging. Both these models are extensions to a first-order kinetic model that has been applied previously to a different foam system [13]. From the best fits of these models to the accelerated aging data, it is possible to predict the long-term behavior (decades) under stockpile conditions. Overall, we find that both for C_S and L_R the long-term predictions for M97* are more consistent as compared to the predictions for M9763. We also find that in both models M9763 is predicted to age more aggressively than M97*, which could possibly be attributed to differences in fillers, differences in desiccation conditions, etc. However, uncertainties remain in terms of the dependencies of model predictions on the level of aging strain, and in the proper interpretation of the activation energy ΔE that come out of the two aging models. In FY 14-15 we would like to tie in the evolution (i.e. aging) of L_R with the time-evolution of C_S and the stress-strain response through a constitutive hyperelastic foam model. Preliminary analysis indicates that an n = 1 or 2 Ogden model [14] might be a good starting point for such an effort.

1.4 Finite-Element Modeling (FEM) of M9763 foams

1.4.1 Background

Polymer foams serve as critical components in the stockpile and our goals are to understand the material behavior and quantify the uncertainty in the mechanical properties of these components over the lifetimes of the relevant systems. When compressed, foams exhibit a stress response determined by both the intrinsic properties of the elastomer and the complex open-cell microstructure. At small strains, the elastic deformation of the structure produces a nearly linear regime, followed by a plateau region indicative of the buckling of cell walls. Further compression eliminates most of the void structure and the stress dramatically increases as the material densifies.

Initial efforts to elucidate the foam structure-property relationships focused on simple geometric unit cells using analytical techniques [15]. More complex geometries assembled from arrays of unit cells are amenable to finite element analysis, though for a given material it is difficult to construct a representative microstructure. The development of X-ray computed tomography (CT) enabled non-destructive detailed characterization of foams and the resulting voxel data can be processed to generate a surface representation for a finite element code [16].

Here, we report a concerted application of X-ray CT and finite element modeling to samples of M9763 foam from a yearlong aging study. Our goals are to enhance our understanding of the complex morphology and mechanical property relationship and to develop the most representative translation of the voxel data into a finite element model. With finite element analysis, we can decouple the aging related alterations to the porous structure from chemical changes in the material microstructure, both of which contribute to changes in the material response. By exploiting analytical aging models and experimental data we can explore the relative contributions of the aged bulk material and porous architectures.

1.4.2 Materials and methods

X-ray CT

Four samples of M9763 were placed between shims within a compression rig with an applied strain of 25% for a 12-month aging study within a room temperature desiccated environment. Each sample was a 10 mm diameter disk with a thickness of 1 mm. At the end of each month, the loaded samples were exposed to an x-ray source for imaging, followed by the removal of the applied strain and a 24-hour relaxation period. The unloaded samples were again imaged to study changes in microstructure and measure the amount of compression set before returning them to a state of 25% compression for another month. Fig. 17 shows images of the reconstructed loaded and unloaded data sliced at the mid-plane to reveal the internal foam structure.

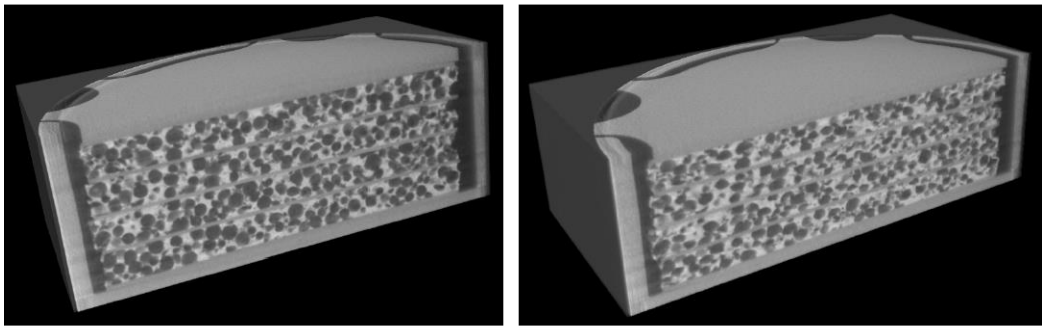

Fig. 17. CT volume renderings of the M9763 samples within the compression rig in the unloaded and loaded states.

Finite element modeling

The raw CT data consisted of a series of images representing consecutive slices of the compression rig and its contents. These images were concatenated to a 3D rendering by the Simpleware visualization software, which also smoothed and segmented the data to extract a voxel-based representation of the foam. With this voxel template, Simpleware converted the data into a tetrahedral volume mesh, which was then translated into finite elements by a custom script designed specifically for this work.

The finite element simulations were performed with Paradyn, a parallel version of the Dyna3D explicit solver, developed at Lawrence Livermore National Laboratory [9]. The domains consisted of an 80×80×1 mm volume extracted from one of the M9763 disks. Two thin plates of a stiff material bounded the upper and lower regions of the domain and provided loading and additional constraints for the simulations; a linear displacement was applied to the upper plate while the lower one remained fixed. The mesh for the foam contained approximately 7 million elements with an average size of 24 microns. The progression from voxel data, to a meshed finite element model is presented in Fig. 18.

To develop a materials model for the simulations, a series of uniaxial cyclic compression tests were conducted of the pure elastomer M9787 from which the foam was produced. Cylindrical specimens with a diameter of 8 mm and a 1.9 mm thickness were compressed in an Instron 5967 at a rate of 0.2 mm/min. A lubricant was applied to the platens to minimize friction. Because of some initial compression set caused by the Mullins effect, the third loading cycle was selected to approximate by the two-parameter Mooney-Rivlin constitutive model,

$$\sigma_{eng} = \left(2C_1 + \frac{2C_2}{\lambda}\right)\left(\lambda - \frac{1}{\lambda^2}\right), \qquad (1.4.1)$$

where $\lambda = 1 + \varepsilon_{eng}$ and the subscript *eng* denotes engineering stress and strain. The model provided an excellent fit to the experimental data (cycle 3 in Fig. 19) and was incorporated into the finite element simulations.

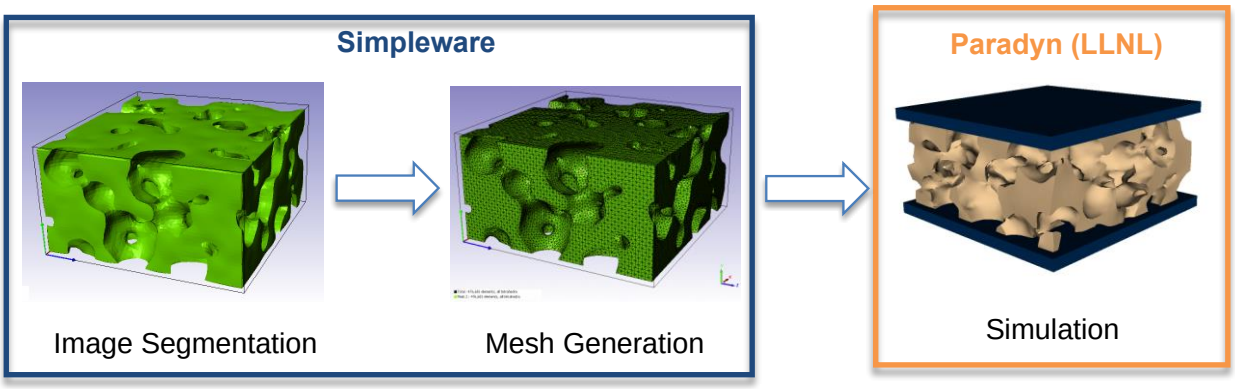

Fig. 18. Depiction of the workflow from the CT data to a finite element mesh.

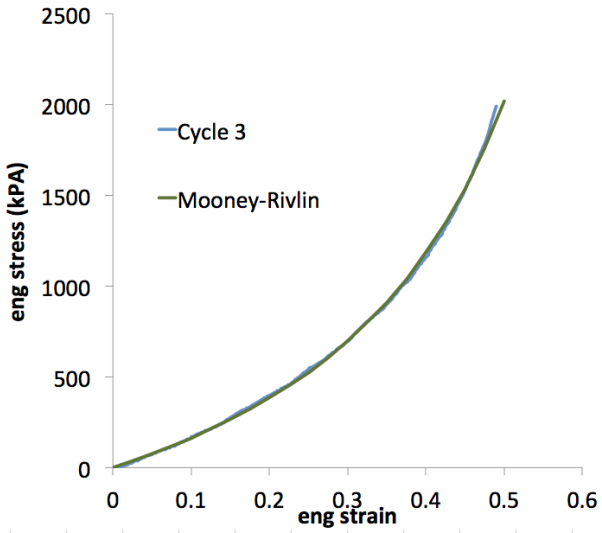

Fig. 19. Comparison of compression data of M9787 with the Mooney-Rivlin model for the finite element simulations.

The applied loading at the top plate was implemented as both a constant velocity and linear displacement. Simulations with the displacement condition ran significantly faster by more than a factor of two. Measurement of the reactive force on the lower fixed plate provided the stress response data.

1.4.3 Results

Fig. 20 shows a representative foam domain at 0% and 40% compression during the finite element simulation. With dynamic simulations we can achieve compressions that exceed 50% before elements deformation exceeds reasonable bounds due to the large contact forces.

The mechanical response from compression is plotted in Fig. 21 for the lower (represented by the blue curves) and upper (represented by the green curves) foam sample in the stack. The solid lines denote the pristine samples and the dashed curves show the response of the aged materials after nine months of desiccation. Some sample

variation is evident (difference between the green and blue solid curves) at compressive strains larger than 15%. However this variability is small when compared to the change in the response after nine months. Both upper and lower foams exhibited softening behavior due to changes in the porous architecture. (At the time of this publication the simulation of the aged upper foam had only run to 6% compression.) Analysis of the CT images revealed the surface to volume ratio of both foams increased after nine months from approximately 11 mm^{-1} to 13 mm^{-1}. Our hypothesis is the desiccated foam becomes more brittle and the repeated unloading and loading provides a damage mechanism whereby new voids form, allowing more air pockets which would reduce the elastic modulus. The formation of more void space is consistent with the increase in surface to volume ratio. A more thorough analysis of the pore size distribution is required to confirm this change in the foam structure.

Fig. 20. Finite element modeling of a CT foam sample under uniaxial compression.

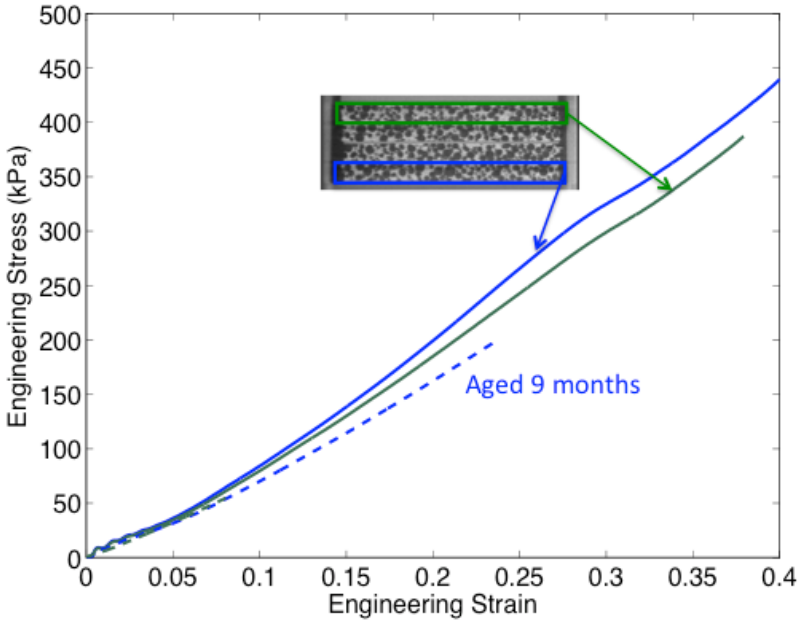

Fig. 21. Foam stress response under uniaxial compression compared with the Mooney-Rivlin constitutive model for the bulk elastomer.

1.4.4 Discussion

We have developed an approach to translate foam CT data into a finite element model in order to investigate the mechanical properties of foams compressed under various aging conditions. With this approach we can decouple the effects of chemical modification of the polymer network and the macroscopic changes in the porous structure. In FY15 we will continue to explore the relationship between morphology and mechanical properties while also quantifying the changes in pore size distribution. Age aware models of the elastomer will also be incorporated in the finite element simulations to help validate constitutive foam models and identify high stress concentration regions.

Acknowledgments:

We would like to thank Ward Small for providing aging data on the various systems discussed in the work above, and Jim Lewicki for providing X-ray CT data on which the finite-element simulations were based. This work was performed under the auspices of the U.S. Department of Energy by Lawrence Livermore National Laboratory under Contract DE-AC52-07NA27344.

1.5 References

1. W. Small *et al.*, *Mechanical property changes in a reinforced silicone elastomer irradiated under tensile strain*, Polym. Degrad. Stab., to be submitted (2014).
2. A. Maiti *et al.*, *Radiation-induced mechanical property changes in filled rubber*, Phys. Rev. E 83, 062801 (2011).
3. A. Maiti *et al.*, *Controlled manipulation of elastomers with radiation: insights from multiquantum nuclear-magnetic-resonance data and mechanical measurements*, Phys. Rev. E 83, 031802 (2011).
4. S. Chinn *et al.*, *Chemical origins of permanent set in a peroxide cured filled silicone elastomer – tensile and ^{1}H NMR analysis*, Polym. Degrad. Stab. 91, 555 (2006).
5. L. Mullins, *Permanent set in vulcanized rubber*, Rubber Chem. Technol. 22, 1036 (1949).
6. J. Diani, et al., *A damage directional constitutive model for Mullins effect with permanent set and induced anisotropy*, Eur J Mech A Solids 25, 483 (2006).
7. R. S. Maxwell et al., *Quantification of radiation induced crosslinking in a commercial, toughened silicone rubber, TR-55 by ^{1}H MQ-NMR*, Polym. Degrad. Stab. 94, 456 (2009).
8. J. Diani et al., *A review on the Mullins effect*, Eur. Polym. J 45, 601 (2009).
9. R. D. Andrews et al., *The theory of permanent set at elevated temperatures in natural and synthetic rubber vulcanizates*, J. Appl. Phys. 17, 352 (1946).
10. A. V. Tobolsky et al., *Stress relaxation of natural and synthetic rubber stocks*, J. Appl. Phys. 15, 380 (1944).
11. A. Maiti et al., *Mullins effect in a filled elastomer under uniaxial tension*, Phys. Rev. E 89, 012602 (2014).
12. M. Patel et al., *Compression set in gas-blown condensation-cured polysiloxane elastomers*, Polym. Degrad. Stab. 95, 2499 (2010).
13. J. E. Coons et al., *A Bayesian analysis of the compression set and stress-strain behavior in a thermally aged silicone foam*, Polym. Degrad. Stab. 91, 1824 (2006).
14. N. Mills, *Polymer Foams Handbook*, Butterworth-Heinemann (Elsevier), Oxford, UK (2010).
15. L. J. Gibson and M. F. Ashby, *Cellular Solids, Structure and Properties*, Cambridge University Press, UK (1999).
16. S. Youssef, E. Maire, and R. Gaertner. *Acta Mater*. 53, 719 (2005).
17. E. Zywicz and J. I. Lin. *DYNA3D: A Nonlinear, Explicit, Three-Dimensional Finite Element Code for Solid and Structural Mechanics: Version 13.1*, Lawrence Livermore National Laboratory, (2013).